Inorg. Chem. **2008**, *47*, 921–929

Strontium Superstoichiometry and Defect Structure of $SrCeO_3$ Perovskite

Glenn C. Mather,*,† Filipe M. Figueiredo,‡,§ Julio Romero de Paz,|| and Susana García-Martín||

Instituto de Cerámica y Vidrio, CSIC, Cantoblanco, 28049 Madrid, Spain, Departamento de Eng. Cerâmica e do Vidro, CICECO, Universidade de Aveiro, Aveiro 3810-193, Portugal, Departamento de Ciências Exactas e Tecnológicas, Universidad Aberta, R. Escola Politécnica 147, 1269-001, Lisbon, Portugal, and Departamento de Química Inorgánica, Facultad de Ciencias Químicas, Universidad Complutense, 28040 Madrid, Spain

Received August 30, 2007

Strontium cerate ($SrCeO_3$) is the parent phase of a family of prototype proton-conducting perovskites with important potential applications as electrolytes in protonic ceramic fuel cells, hydrogen-separation membranes, and sensors for hydrogen and humidity. Apparent nonstoichiometric behavior and the microstructure of $SrCeO_3$ have been investigated. Phase analysis by X-ray diffraction indicates that single-phase material in the system $Sr_{1+x}CeO_{3+\delta}$ is obtained for compositions $x = 0.02–0.03$ and that nominally stoichiometric $SrCeO_3$ ($x = 0$) synthesized by either solid-state reaction or the citrate method is Sr-rich. Selected area electron diffraction confirms that the system crystallizes with the $GdFeO_3$-type orthorhombic perovskite structure (space group *Pnma*). Structural defects characterized by high-resolution transmission electron microscopy include twin domain boundaries and SrO-rich, Ruddlesden–Popper-type planar defects. Magnetic susceptibility measurements down to 2 K indicate that the Ce^{3+} content is minor (~0.01 mol per formula unit for slow-cooled material) and does not influence the observed nonstoichiometry.

Introduction

Strontium cerate is the parent phase of a widely studied perovskite (ABO_3) family of considerable fundamental and technological interest for exhibiting moderately high proton conductivity ($>10^{-3.5}$ S·cm^{-1} at 650 °C).[1−5] Incorporation of protons takes place in wet or hydrogen-containing atmospheres substituting Ce^{4+} with a lower valence cation, typically Y^{3+} or Yb^{3+}. The charge-compensating oxygen vacancies are filled with a hydroxyl group from a water molecule and the corresponding proton forms a second hydroxyl group with a lattice oxygen. Poor stability related to reaction with CO_2 is one problem which may hinder the use of these materials in commercial electrochemical devices, such as fuel-cell electrolytes and hydrogen-separation membranes.[6] Moreover, reports indicate that $SrCeO_3$ is thermodynamically unstable with respect to the constituent oxides at room temperature.[7,8]

We recently studied nonstoichiometry in strontium cerate, $Sr_{1+x}CeO_{3+\delta}$, over the composition range $-0.02 \le x \le 0.04$.[9] An objective of the study was to introduce Sr deficiency to improve the poor stability of $SrCeO_3$-based phases, either through lowering the Sr chemical potential or depleting the grain boundaries of trace amounts of reactive SrO. In principle, the creation of cation vacancies in this system could be charge-compensated by oxygen vacancies to provide a dopant-free route to proton absorption; however, strontium-deficient perovskite was not obtained.

Instead, nominally stoichiometric $SrCeO_3$ was found to be slightly Sr-rich (or Ce-deficient) over the studied temperature range (1100−1450 °C); CeO_2 was consistently

* To whom correspondence should be addressed. E-mail: mather@icv.csic.es.
† CSIC.
‡ Universidad Aveiro.
§ Universidad Aberta.
|| Universidad Complutense.

(1) Uchida, H.; Maeda, N; Iwahara, H. *Solid State Ionics* **1983**, *11*, 117.
(2) Marnellos, G.; Stoukides, M. *Science* **1998**, *282*, 98.
(3) Kumar, R. V. *J. Alloys Compd.* **2006**, *408*, 463.
(4) Mather, G. C.; Islam, M. S. *Chem. Mater.* **2005**, *17*, 1736.
(5) Song, S.-J.; Wachsman, E. D.; Dorris, S. E.; Balachandran, U. *J. Electrochem. Soc.* **2003**, *150*, A790.
(6) Scholten, M. J.; Schoonman, J.; van Miltenburg, J. C.; Oonk, H. A. J. *Solid State Ionics* **1993**, *61*, 83.
(7) Gopalan S.; Virkar, A. V. *J. Electrochem. Soc.* **1993,** *140*, 1060.
(8) Shirsat, A. N.; Kaimal, K. N. G.; Bharadwaj, S. R.; Das, D. *J. Solid State Chem.* **2004**, *177*, 2007.
(9) Mather, G. C.; Jurado J. R. *Bol. Soc. Esp. Cerám. Vidrio* **2003**, *42*, 311.

10.1021/ic701703c CCC: $40.75
Published on Web 01/01/2008

observed in X-ray diffraction (XRD) patterns as a second phase for $x = 0$. Structural refinements[9] of the range of $Sr_{1+x}CeO_{3+\delta}$ compositions by Rietveld analysis of powder X-ray diffraction data based on stoichiometric $SrCeO_3$ were consistent with the previously reported, average structure.[10,11]

It is widely recognized that real crystalline solids are usually much more complex than the simple periodic arrangement of ions routinely accessible by X-rays or neutrons. Microstructural phenomena such as microdomain formation and trapping effects have an important influence on the electrical performance of ionic or mixed conductors.[12−15] Anomalous variations in the unit-cell parameters of $ACeO_3$-type (A = Ba, Sr) solid solutions highlight the complexity of these systems, in particular, where defect association, hydration effects, and the "amphoteric" site preference of dopants may be expected.[4,16] Although solid-state, high-temperature proton conductors are an important class of materials for many electrochemical applications, little attention has been paid to their microstructure. High-resolution transmission electron microscopy (HRTEM) is one tool that may assist in exposing microstructural features that are not apparent at the resolution of neutrons or laboratory X-rays.[17]

In this report, the apparent nonstoichiometry and microstructure of $SrCeO_3$ are investigated. Particular attention is paid to the compositional range, thermal stability, and defect structure of Sr-excess material that appears to form, even for the nominally stoichiometric composition. Selected area electron diffraction is employed to confirm the orthorhombic perovskite crystal structure of the $SrCeO_3$ system, whereas HRTEM analyzes defect phenomena and microstructure at a resolution above that which has previously been reported. The Ce oxidation state is evaluated using SQUID magnetic-susceptibility measurements down to 2 K.

Experimental Section

Compositions in the $Sr_{1+x}CeO_{3+\delta}$ system ($0 \le x \le 0.2$) were prepared by solid-state reaction from $SrCO_3$ (99.9%, dried at 300 °C) and CeO_2 (99.9%, dried at 600 °C) in appropriate ratios. The reagents were first ball-milled for 2 h in isopropyl alcohol, dried, and fired at 1100 °C for 12 h. The powders were then milled in acetone and fired at 1200 °C for 24 h with intermediate grinding. The standard synthesis procedure involved final firing at 1350 °C for 48 h with a heating rate of 5 °C min^{-1} and a cooling rate of 1 °C min^{-1}; higher firing temperatures (e.g., 1400 °C for 36 h) were also employed to verify reaction completion. Selected samples of the prepared material were subject to additional thermal treatment to determine high- and low-temperature phase equilibria. Annealing was conducted in the temperature range 550−850 °C for periods up to 11 days followed by slow cooling to room temperature at 0.5 °C min^{-1} or quenching in air was performed from temperatures in the range 1250−1350 °C.

The citrate process was also employed as a check on phase formation. A similar procedure to that reported for the synthesis of $BaCeO_3$ was followed.[18] Citric acid (0.2 mol) and ethylene glycol (0.8 mol) were first heated and stirred at 50 °C for 40 min. $Ce(NO_3)\cdot 6H_2O$ (0.02 mol) was added to the mixture, which was heated and stirred for a further 30 min; then $Sr(NO_3)_2$ was added and the temperature was raised and maintained at 80 °C for 5 h, with continuous stirring. This solution was subsequently heated at 90 °C for 18 h to obtain a dark brown polymerized complex. Further heat treatment involved pyrolysis in the temperature range 275−400 °C, with final firing at 1100 °C for 4 h.

Completeness of reaction and phase purity were examined by powder X-ray diffraction (XRD) with a Siemens D5000 diffractometer using Cu Kα radiation. A typical slow scan employed for phase analysis was conducted in the range $15° \le 2\theta \le 40°$ (step width, 0.02°), giving a maximum reflection intensity of several thousand counts. These scan parameters were adopted to allow the identification of small quantities ($\lesssim$3 mol %) of second phases.

The chemical composition was verified by inductively coupled plasma atomic emission spectroscopy (ICP-AES) with a Jobin Yvon 70 Plus spectrometer (Horiba Jobin Yvon Inc., Edison, NJ). Sample preparation involved treatment of the material in a microwave chamber CEM MDS-8 I D (CEM Corporation, Matthews, NC) with a mixture of hydrochloric and nitric acids and subsequent dilution. Reproducibility was ensured by repeating measurements for different diluted solutions. The calibration curve was based on six pattern solutions. We note that the precision of ICP-AES is in the ppm range, which is sufficient to securely detect compositional differences of 0.01 mol %.

For transmission electron microscopy, samples were ground in *n*-butyl alcohol and ultrasonically dispersed. A few drops of the resulting suspension were deposited on a carbon-coated grid. SAED and HRTEM studies were performed with a JEOL 3000EX electron microscope (double tilt ±20°) working at 300 kV.

Magnetic measurements were performed on polycrystalline samples using a SQUID magnetometer (Quantum Design, model MPMS-XL). The temperature dependence of magnetization (M) was measured in the temperature range 2−100 K at an applied magnetic field (H) of 0.05 T upon heating samples under zero-field-cooled conditions from 2 K (previously cooled at $H = 0$ T). The experimental molar magnetic susceptibility χ_{exp} (M/H) was calculated on the basis of the sample mass (∼56 mg) and the molecular weight (277.81 g mol^{-1}). The molar paramagnetic susceptibility χ_p was then obtained on subtraction of the diamagnetic contribution from each ion; the susceptibility values were taken as -15×10^{-6}, -17×10^{-6}, and -12×10^{-6} emu mol^{-1} for Sr^{2+}, Ce^{4+}, and O^{2-} ions, respectively.[19] We note that SQUID magnetometers are one of the most sensitive methods to detect paramagnetic species such as Ce^{3+} ions ([Xe] $4f^1$ electron configuration), and that measurement of the paramagnetic susceptibility is a proven analytical tool for determining the concentration of paramagnetic species.

Results

Phase Analysis. On final firing, all compositions formed perovskite $SrCeO_3$ with an orthorhombic unit cell (space

(10) Knight, K. S.; Bonanos, N. *Mater. Res. Bull.* **1995**, *30*, 347.
(11) Ranlov, J.; Lebech, B.; Nielsen, K. *J. Mater. Chem.* **1995**, *5*, 743.
(12) Kilner, J. A.; Steele, B. C. H. *J. Electrochem. Soc.* **1982**, *C143−148*, 129.
(13) Irvine, J. T. S.; Feighery, A. J.; Fagg, D. P.; García-Martín S. *Solid State Ionics* **2000**, *136−137*, 879.
(14) Figueiredo, F. M.; Kharton, V. V.; Waerenborgh, J. C.; Viskup, A. P.; Naumovich, E. N.; Frade, J. R. *J. Am. Ceram. Soc.* **2004**, *87*, 2252.
(15) Ruiz-Morales, J. C.; Canales-Vázquez, J.; Savaniu, C.; Marrero-López, D.; Zhou, W.; Irvine, J. T. S. *Nature* **2006**, *439*, 568.
(16) Kruth, A.; Mather, G. C.; Jurado, J. R.; Irvine, J. T. S. *Solid State Ionics* **2005**, *176*, 703.
(17) García-Martín, S.; Alario-Franco, M. A.; Ehrenberg, H.; Rodríguez-Carvajal, J.; Amador, U. *J. Am. Chem. Soc.* **2004**, *126*, 3587.
(18) Lee, D. W.; Won, J. H.; Shim, K. B. *Mater. Lett.* **2003**, *57*, 3346.
(19) Mulay, N.; Boudreaux, E. A. *Theory and Applications of Molecular Paramagnetism*; Wiley-Interscience: New York, 1976.

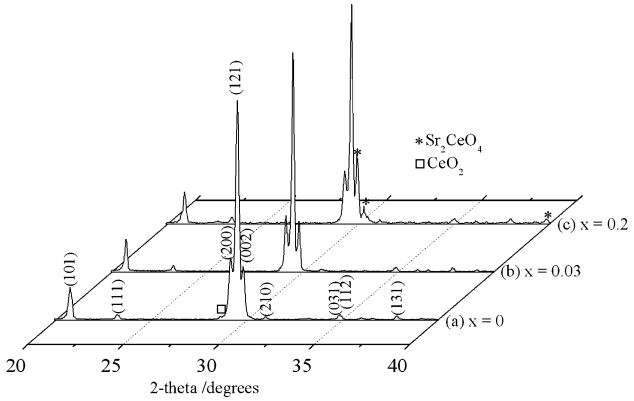

Figure 1. X-ray powder diffraction patterns of the $Sr_{1+x}CeO_{3+x}$ system: (a) $x = 0$ synthesized by the citrate process with final firing at 1100 °C; (b) $x = 0.03$ synthesized by solid-state reaction with final firing at 1350 °C; (c) $x = 0.2$ synthesized by solid-state reaction with final firing at 1350 °C (all samples were slow-cooled to room temperature). Selected indexing in space group *Pnma* is shown.

group *Pnma*) as the principal phase;[9−11] lattice parameters for nominally stoichiometric $SrCeO_3$, taken from ref 9, are $a = 6.13117(6)$, $b = 8.56042(9)$, and $c = 5.9945(6)$ Å. In accordance with earlier studies,[9,20] CeO_2 was identified as a second phase in nominally stoichiometric $SrCeO_3$ synthesized by both the citrate process, with final firing at 1100 °C (Figure 1a), and solid-state reaction, with final firing in the range 1350−1400 °C, followed by either slow cooling or quenching.

X-ray phase-pure material was obtained for compositions $Sr_{1.02}CeO_{3.02}$ and $Sr_{1.03}CeO_{3.03}$ on firing at 1350 °C for 48 h and slow cooling at 1 °C min^{-1} (Figure 1b). For $Sr_{1.04}CeO_{3.04}$, vestiges of Sr_2CeO_4 could be discerned, the identification of which by X-ray diffraction is problematic due to the overlap of its principal reflections with strong reflections of $SrCeO_3$ (29.5−30° 2θ). The presence of Sr_2CeO_4 was unambiguously observed in the composition $x = 0.2$ however (Figure 1c). Our earlier study[9] indicated that $Sr_{1.04}CeO_{3.04}$ could be obtained (XRD) phase-pure at 1350 °C. Nonetheless, a solid piece sintered at 1400 °C disintegrated after several hours' exposure to the laboratory air, suggesting that carbonation or hydration of excess Sr had occurred. We note that, commonly, the presence of only a very small amount of unreacted basic oxide is sufficient to bring about disintegration of the sintered body. For lower Sr contents ($x < 0.04$), the mechanical integrity of ceramic bodies was retained indefinitely.

The X-ray diffraction patterns of $Sr_{1.02}CeO_{3.02}$ are shown in Figure 2a upon first (i) slow cooling from 1350 °C, then (ii) annealing at 850 °C for 11 days followed by slow cooling at 0.5 °C min^{-1}, and finally (iii) quenching of the annealed sample from 1350 °C. The XRD pattern of $Sr_{1.02}CeO_{3.02}$ slow-cooled from 1350 °C is single phase, whereas the annealed sample shows some evidence of the formation of Sr_2CeO_4, which includes the growth of a small broad feature at ∼30.5° 2θ; additionally, the relative intensity of the (0 0 2) reflection, around the same region as the strongest Sr_2CeO_4 reflections, apparently increases with respect to that

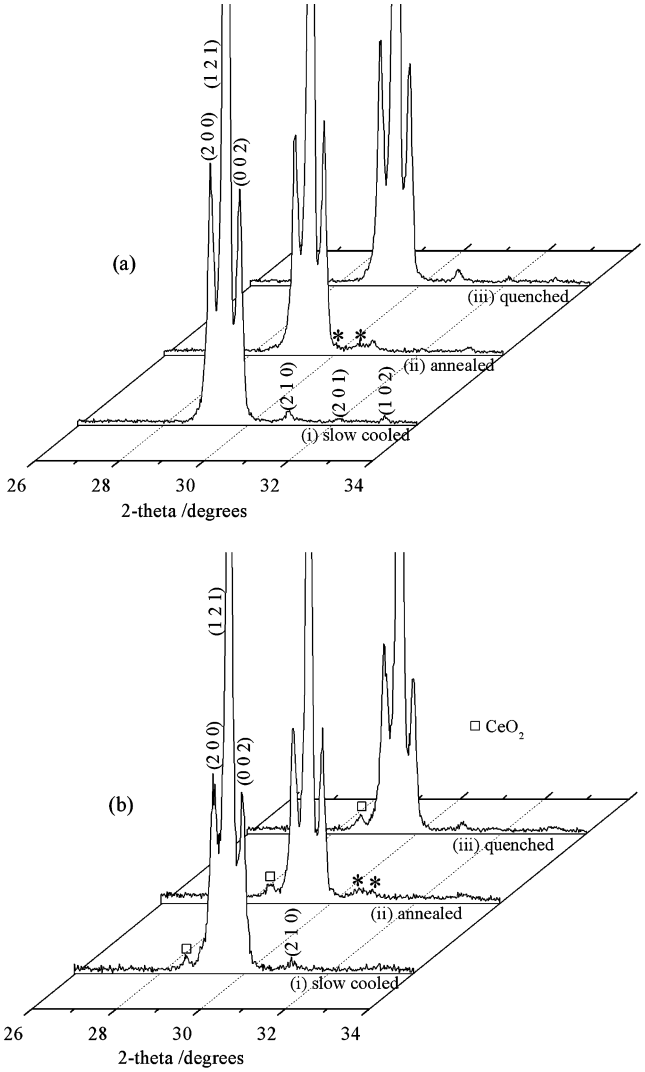

Figure 2. X-ray powder diffraction patterns: (a) $Sr_{1.02}CeO_{3.02}$ after sequential (i) slow cooling from 1350 °C at 1 °C min^{-1}, (ii) annealing at 850 °C for 11 days followed by slow cooling at 0.5 °C min^{-1}, and (iii) quenching of the annealed sample in air from 1350 °C; (b) $SrCeO_3$ after (i) slow cooling from 1400 °C, (ii) annealing at 850 °C for 11 days followed by slow cooling at 0.5 °C min^{-1}, and (iii) quenching from 1250 °C. Selected indexing in space group *Pnma* is shown; asterisks indicate possible formation of Sr_2CeO_4.

of (2 0 0). On quenching of the annealed sample from 1350 °C (Figure 1a(iii)), the XRD pattern is once more equivalent to that of the unannealed material.

Similar behavior is observed for nominally stoichiometric $SrCeO_3$ (Figure 2b). A broad feature also develops on annealing at ∼30−35° 2θ in the XRD pattern, which subsequently disappears on quenching from high temperature. We note that CeO_2 persists in the XRD patterns at each stage of the thermal history of $SrCeO_3$.

The Sr:Ce molar ratio of $Sr_{1+x}CeO_{3+\delta}$ ($0 \le x \le 0.02$) determined by ICP-AES (Table 1a) is in good agreement with the nominal stoichiometry. The sensitivity of the technique to minor variations in the cation stoichiometry provides an important confirmation of the differences in phase composition. The present results of powdered samples are in accord with compositional analysis by electron probe microanalysis (EPMA) of sintered bodies of a range of

(20) Chavan, S. V.; Tyagi, A. K. *Thermochim. Acta* **2002**, *390*, 79.

Table 1. Compositional Analyses of the $Sr_{1+x}CeO_{3+x}$ System

(a) Comparison of Nominal and ICP-AES Measured Sr:Ce Molar Ratio

	Sr:Ce molar ratio	
composition (x)	nominal	ICP-AES[a]
0	1	0.991
0.02	1.02	1.027
0.03	1.03	1.034

(b) Sr:Ce Molar Ratio of Main Perovskite Phase Measured by EPMA[9]

composition (x)	nominal	EPMA of main phase
−0.02	0.98	1.04(3)
0	0	1.021(3)
0.04	1.04	1.043(7)

[a] Errors are associated with the third decimal place.

compositions ($-0.02 \leq x \leq 0.04$), which indicated Sr excess in the main (perovskite) phase for all x;[9] these data are reproduced in Table 1b.

Selected Area Electron Diffraction and High-Resolution Transmission Electron Microscopy. Three selected area electron diffraction (SAED) patterns along different zone axes of $Sr_{1.02}CeO_{3.02}$, annealed at 1350 °C and cooled at 1 °C min^{-1}, are shown in Figures 3a−3c. The patterns are indexed according to the ideal cubic perovskite cell (indicated as p). In addition to the strong Bragg reflections characteristic of the perovskite structure, both in-phase tilt and anti-phase tilt superlattice reflections appear. In-phase tilt reflections, $^1/_2$ $(oeo)_p$ $h \neq l$ ("o" indicates a Miller index with an odd number and "e" with even number), are indicated with an arrow in the pattern of the $[010]_p$ zone axes (Figure 3a); anti-phase tilt superlattice reflections, $^1/_2$ $(ooo)_p$, are similarly indicated in the pattern of the $[01\bar{1}]_p$ zone axis (Figure 3c). These reflections arise from mixed tilting of the octahedral CeO_6 network ($a^-b^+a^-$ tilt system, Glazer's notation[21,22]) in

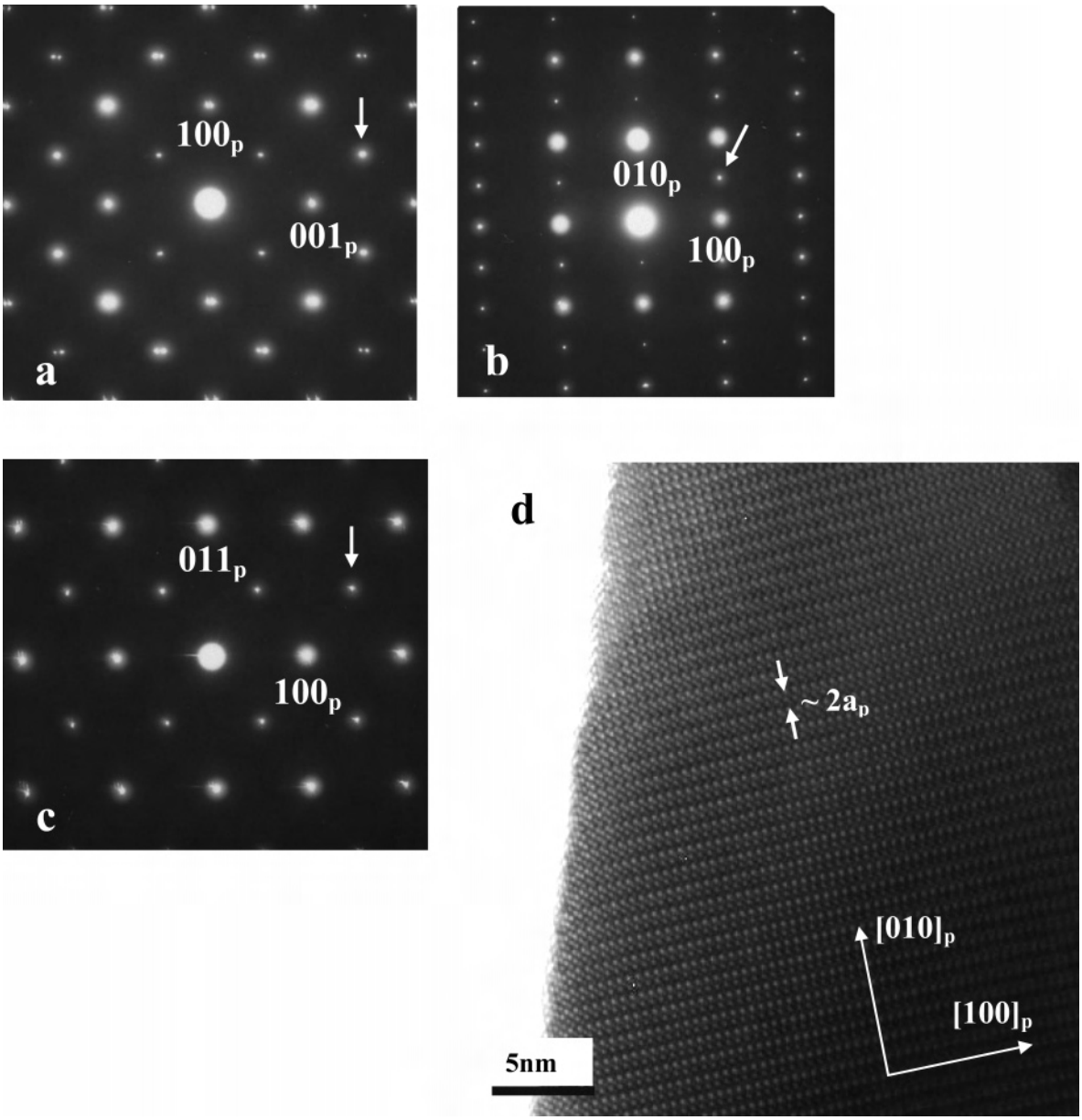

Figure 3. Selected area electron diffraction patterns of $Sr_{1.02}CeO_{3.02}$ fired at 1350 °C and slow-cooled to room temperature projected along the (a) $[010]_p$, (b) $[001_p]$ and (c) $[01\bar{1}]_p$ zone axes; (d) HRTEM image corresponding to the $[001]_p$ zone axis.

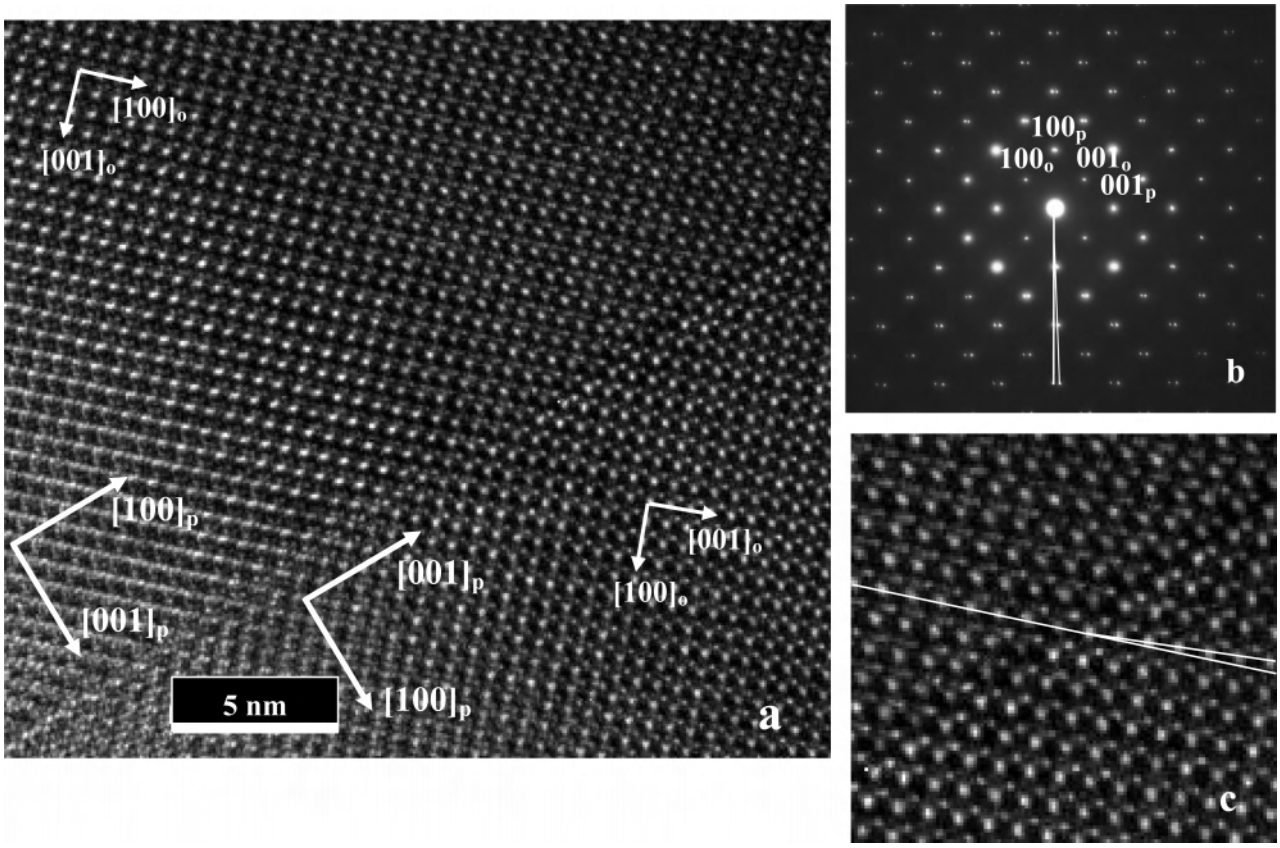

Figure 4. (a) HRTEM image of $Sr_{1.02}CeO_{3.02}$ annealed at 1350 °C and slow-cooled to room temperature; (b) corresponding SAED pattern projected along the $[010]_p$ zone axis and (c) magnification of the HRTEM image. The corresponding orthorhombic Miller indices and crystallographic directions are indicated in the diffraction pattern and HRTEM image, respectively.

agreement with the *Pnma* space group determined for the $SrCeO_3$ system from powder neutron and X-ray diffraction studies.[10,11]

Moreover, $^1/_2$ $(eoe)_p$ reflections can be observed, such as the $^1/_2$ $(210)_p$ reflection in the pattern along the $[001]_p$ zone axis (Figure 3b). These reflections may be attributable either to antiparallel cation displacements within the A positions of the perovskite structure (i.e., shifts of the Sr ions) or to the combination of in-phase and anti-phase tilting ("concert" reflections).[23] The $^1/_2$ $(210)_p$ reflection is rather weak, and not observable by X-ray diffraction, which suggests that it arises from the latter phenomenon. The 1/2 $(0k0)_p$, 1/2 $(101)_p$, and $^1/_2$ $(111)_p$ reflections arise as a consequence of double diffraction; the respective origins of the secondary diffraction patterns are the $^1/_2$ $(210)^*_p$, $^1/_2$ $(103)^*_p$, and $^1/_2$ $(311)^*_p$ positions in reciprocal space. The HRTEM image corresponding to the $[001]_p$ zone axis is shown in Figure 3d; the contrast differences with a periodicity of $\sim 2a_p$ are consistent with the orthorhombic $\sim\sqrt{2}a_p \times \sim 2a_p \times \sim\sqrt{2}a_p$ unit cell.

The HRTEM image along the$[010]_p$ zone axis and corresponding SAED pattern are shown in Figures 4a and 4b. Splitting of all the reflections is clearly observed in the SAED pattern (also observed in Figure 3a). This splitting is due to twinning which gives rise to two domains with a common $[010]_p$ axis (co-incident with the orthorhombic $[010]_o$ axis) in which the a_p and c_p (also a_o and c_o) are interchanged;[24−26] the twin planes are $\{100\}_p$ (i.e., $\{101\}_o$). The two domains are separated by a twin boundary weakly visible as a contrast line along the $[100]_p$ direction (corresponding to $[001]_p$ in the adjacent domain), consistent with the SAED pattern. The angle θ between the a_o and c_o axes at both sides of the twin boundary, which is indicated in the magnified HRTEM image (Figure 4c) and the SAED pattern, is given by $\theta = 2\text{arctg}(c_o/a_o)$.[25]

A large number of crystals exhibit the pattern shown in Figure 5a, which is projected along the $[001]_p$ zone axis. One interpretation of the origin of the pattern could be the superposition of the diffraction of three mutually perpendicular domains, as observed in $CaTiO_3$ [24] and other oxides with perovskite-type structures.[17] However, such a microstructure should also result in contrast differences with a periodicity $\sim 2a_p$ along perpendicular directions in different regions of the crystal in the corresponding HRTEM images; contrast differences of this nature are not observed in this case. Instead, the corresponding HRTEM image reveals a different type of microstructural feature in which domains are related by a displacement of $^1/_2$ of the unit cell along the $[010]_p$ direction, as indicated in Figure 5b by black lines.

(21) Glazer, A. M. *Acta Crystallogr.* **1972**, *B28*, 3384.
(22) Glazer, A. M. *Acta Crystallogr.* **1975**, *A31*, 756.
(23) Woodward, D. I.; Reaney, I. M. *Acta Crystallogr.* **2005**, *B61*, 387.
(24) White, T. J.; Segall, R. L.; Barry, J. C.; Hutchison, J. L. *Acta Crystallogr.* **1985**, *B41*, 93.
(25) Zandbergen, H. W.; van Tendeloo, G.; Okabe, T.; Amelinckx, S. *Phys. Status Solidi* **1987**, *103*, 45.
(26) Chaillout, C.; Gautier, E.; Kopnin, E. M.; Fournier, T.; Antipov, E. V.; Marezio, M. *J. Solid State Chem.* **1996**, *123*, 236.

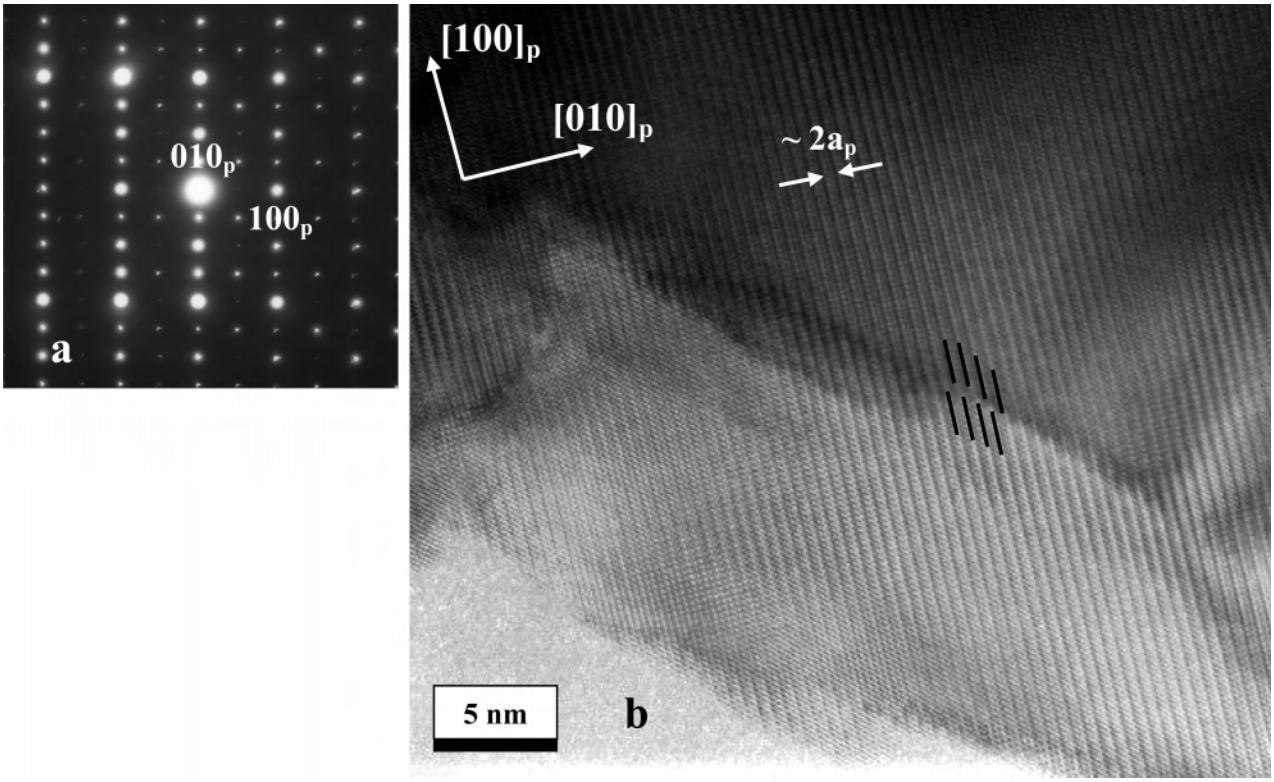

Figure 5. (a) SAED pattern of $Sr_{1.02}CeO_{3.02}$ (fired at 1350 °C and slow-cooled to room temperature) projected along the $[001]_p$ zone axis and (b) the corresponding HRTEM image.

These domain boundaries are consistent with Ruddlesden−Popper (RP) planar defects.[27,28] The boundaries are rather irregular as is the case for the RP defects observed by Yang et al.[27] in the $BiMnO_3$ system. The pattern in Figure 5a arises as a consequence of the superposition of the patterns of the two domains translated by half a unit cell with respect to one another by the RP domain boundary. An alternative explanation of the image contrast of Figure 5b as being the result of a change in thickness would not give rise to the corresponding diffraction pattern.

Similar domain boundaries were observed in all crystals of $Sr_{1.02}CeO_{3.02}$ samples with different thermal treatments (slow-cooled or quenched in air from 1350 °C, or annealed at 850 °C for 11 days and then slow-cooled) and $SrCeO_3$ with the ideal composition. The very large number of examined crystals indicates that these domain boundaries are a characteristic feature of $SrCeO_3$ pervoskites rather than an artifact in the image contrast. We note that it is impossible to establish any meaningful correlation between the number of defects and composition because of the limited compositional variance in the $Sr_{1+x}CeO_{3+\delta}$ system ($x = 0.02-0.03$).

Magnetic Measurements and Ce Oxidation State. To determine the presence of Ce^{3+} ions, magnetic susceptibility measurements were performed at low temperatures on samples of $Sr_{1.02}CeO_{3.02}$ with varied thermal histories. The data provide evidence of paramagnetic species in samples that were slow-cooled at 1 °C min^{-1} from 1350 °C or quenched in air from the same temperature (Figure 6). In the case of a sample annealed at 850 °C and slow-cooled to room temperature, no paramagnetic signal is obtained at 2 K (data not shown). The molar paramagnetic susceptibility (χ_p) of the quenched sample exhibits higher values with respect to those of the slow-cooled material, indicating a higher concentration of paramagnetic species. This is most likely due to the partial reduction of Ce^{4+} to Ce^{3+} associated with entropically driven oxygen loss at high temperature. The temperature dependence of the reciprocal molar paramagnetic susceptibility (χ_p^{-1}) of the quenched sample, shown in the inset of Figure 6, is composed of two distinct regimes.

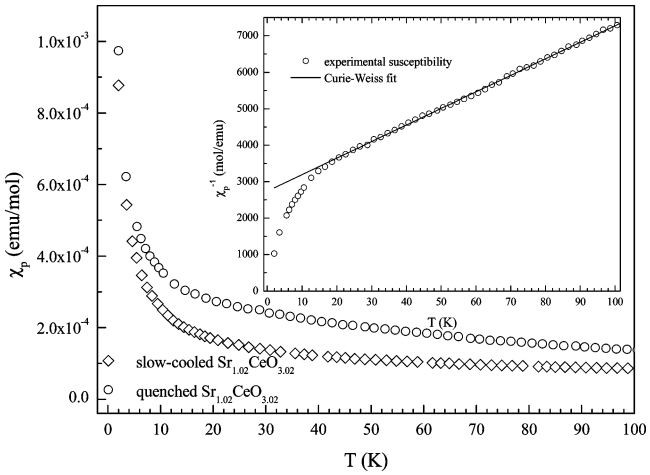

Figure 6. Temperature dependence of the magnetic susceptibilities of slow-cooled and quenched $Sr_{1.02}CeO_{3.02}$ (both from 1350 °C). The inset shows the inverse susceptibility as a function of temperature for the quenched sample. The solid line represents the fit to the Curie−Weiss law.

(27) Yang, H.; Chi, Z. H.; Yao, L. D.; Zhang, W.; Li, F. Y.; Jin, C. Q.; Yu, R. C. *J. Appl. Phys.* **2006**, *100*, 044105.
(28) Wu, J. S.; Jia, C. L.; Urban, K.; Hao, J. H.; Xi, X. X. *J. Cryst. Growth* **2002**, *234*, 603.

From 100 K down to nearly 20 K, the behavior is linear and obeys the Curie−Weiss law $\chi = C/(T - \theta)$, where C is the Curie constant and θ the Weiss temperature. On fitting of data in this range accordingly, values of $C = 2.206(9) \times 10^{-2}$ emu K mol^{-1} and $\theta = -60.4(5)$ K are obtained. Below 20 K, a significant negative deviation from the Curie−Weiss law is observed, attributable to the presence of a trivalent rare-earth ion with an odd number of 4f electrons, in this case Ce^{3+}. Similar magnetic behavior has been found in several compounds with cerium in the trivalent state.[29−31] It is well-established that the nonlinear behavior of the magnetic susceptibility at low temperatures originates from the energy splitting of the ground state of the Ce^{3+} ion, the J multiplet $^2F_{5/2}$, under the crystalline electric field of the neighboring ions. Similar results were obtained for the slow-cooled sample; data from 100 to 20 K fitted to the Curie−Weiss law yielded values of $C = 3.15(7) \times 10^{-3}$ emu K mol^{-1} and $\theta = -8.5(6)$ K.

As mentioned earlier, the analysis of the magnetic susceptibility may allow the concentration of the paramagnetic Ce^{3+} ion to be determined. However, this is only possible when an expected theoretical or experimental value of its effective magnetic moment or Curie constant is available. The free Ce^{3+} ion has a theoretical effective magnetic moment $\mu_{eff} = 2.54\ \mu_B$, corresponding to the ground-state multiplet $^2F_{5/2}$ since $\mu_{eff} = g_J\sqrt{J(J+1)}$, where the so-called Landé splitting factor g_J has a value of $^6/_7$ and $J = {}^5/_2$. However, for an f^1 electron (Ce^{3+}, Pr^{4+}, Pa^{4+}, U^{5+}, or Np^{6+}), the Landé factor is likely to be affected by interaction with the crystal field, which may significantly reduce the effective magnetic moment to a value as low as $0.68\ \mu_B$.[32,33] Therefore, to determine quantitatively the Ce^{3+} ion in the $Sr_{1.02}CeO_{3.02}$ samples, we have assumed that its expected effective magnetic moment is $1.57\ \mu_B$, equivalent to the effective magnetic moment determined for isostructural $SrPrO_3$.[34] Thus, considering that $\mu_{eff} = \sqrt{8C}$, the quantity of Ce^{3+} ions can be calculated by dividing the experimental Curie constant obtained for each sample by the expected value. Accordingly, the quenched and slow-cooled samples are found to contain 0.072(1) and 0.010(2) mol of Ce^{3+} per formula unit, respectively.

Discussion

Thermodynamic studies[7,8] demonstrate that $SrCeO_3$ exhibits positive values of both enthalpy and entropy and is, thus, unstable relative to its constituent oxides at low temperatures. Gopalan and Virkar[7] indicate that the lower stability limit is $\gtrsim$ 366 °C, whereas Shirsat et al.[8] specify that this temperature is higher, ∼750 °C. It has also been reported that $SrCeO_3$ does not form below 950 °C, but that Sr_2CeO_4 and CeO_2 constitute the low-temperature phase equilibria.[35]

There are numerous studies that highlight the difficulty of preparing phase-pure $SrCeO_3$ perovskite. Cordfunke et al.[36] state that, despite repeated heating cycles, a small amount of CeO_2 persists in the XRD patterns of $SrCeO_3$. In other diffraction studies, the region of the most intense CeO_2 reflection is omitted from refinement,[11] or comparatively large residuals are observed in the Rietveld difference profile.[10] In addition to our earlier work,[9] a recent, independent investigation by Chavan and Tyagi[20] also reports the presence of CeO_2 impurity in "$SrCeO_3$" and indicates that the regime for Sr excess extends to greater SrO concentrations ($x \sim 0.5$). The present phase analyses, which reveal that CeO_2 exists as a second phase on synthesis of $SrCeO_3$ by solid-state reaction or the citrate process, are thus entirely consistent. In contrast to these reports,[9,20,36] other authors, in a detailed electrical conductivity study,[37] claim that a solid solution forms for compositions in the range $0.98 \le x \le 1.10$ for $Sr_xCeO_{3-\delta}$, although no diffraction patterns or microscopy data were provided. We note that, to the best of our knowledge, no structural study of single-crystal $SrCeO_3$ has been performed.

As discussed previously,[8,9] the instability of $SrCeO_3$ may arise from the mismatch of the relatively small Sr and large Ce ionic radii on the A and B perovskite sites, respectively ($^{XII}r_{Sr}{}^{2+} = 1.44$ Å, $^{VI}r_{Ce}{}^{4+} = 0.87$ Å).[38] This places the Goldschmidt tolerance factor of $SrCeO_3$, $t \sim 0.804$, in the lower range for observed $A^{2+}B^{4+}O_3$ perovskites.[39,40] (The tolerance factor was calculated as $t = (r_A + r_B)/(\sqrt{2}(r_A + r_B))$ where r_A, r_B, and r_O are the ionic radii of A, B, and O, respectively, in VI-fold coordination;[38,39] note that other authors calculate t based on r_A in a higher coordination environment.) Yokokawa et al.[40] have correlated a lower tolerance factor with a smaller enthalpy of formation of perovskites from the binary oxides. In this respect, although we may assume that the small quantity of detected Ce^{3+} resides on one or both of the regular A or B cation lattice sites, the presence of significant amounts of Ce^{3+} on the B site would lead to a lower Goldshmidt tolerance factor and still lower stability. We may also exclude a considerable presence of Ce^{3+} on the A site since this situation would tend to accommodate Sr deficiency rather than Sr excess, contrary to experiment. It follows, therefore, that the amount of Ce^{3+} in the $SrCeO_3$ system is minor, in accordance with the magnetic data.

In spite of the thermodynamic instability of $SrCeO_3$, the system displays a high degree of metastability, as indicated by our phase analyses after long-term annealing in the range

(29) Hoehn, M. V.; Karraker, D. G. *J. Chem. Phys.* **1974**, *60*, 393.
(30) Guo, M. D.; Aldred, A. T.; Chan, S. K. *J. Phys. Chem. Solids* **1987**, *48*, 229.
(31) Aricó, E. M.; Kanellakopulos, B.; Apostolidis, C.; Zinner L. B. *J. Alloys Compd.* **1998**, *275−277*, 798.
(32) Bickel, M.; Goodman, G. L.; Soderholm, L.; Kanellakopulos, B. *J. Solid State Chem.* **1994**, *76*, 178.
(33) Hinatsu, Y.; Edelstein, N. *J. Solid State Chem.* **1994**, *112*, 53.
(34) Hinatsu, Y.; Itoh, M.; Edelstein, N. *J. Solid State Chem.* **1996**, *132*, 337.
(35) Fu, S. L.; Dai, J.; Ding, Q. K. *J. Inorg. Mater.* **2006**, *21*, 357 (in Chinese).
(36) Cordfunke, E. H. P.; Booij, A. S.; Huntelaar, M. E. *J. Chem. Thermodyn.* **1998**, *30*, 437.
(37) Shimura, T.; Ma, G.; Matsumoto, H.; Iwahara, H. *Electrochemistry* **2000**, *68*, 439.
(38) Shannon, R. D. *Acta Crystallogr.* **1976**, *A32*, 751.
(39) Li, C.; Kwan Soh, K. C.; Wu, P. *J. Alloys Compd.* **2004**, *372*, 40.
(40) Yokokawa, H.; Kawada, T.; Dokiya, M. *J. Am. Ceram. Soc.* **1989**, *72*, 152.

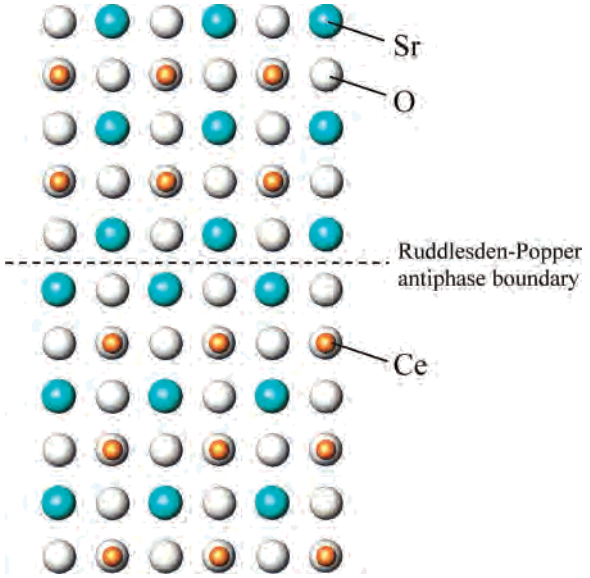

Figure 7. Projection of a $\{1\ 0\ 0\}_p$ layer of $SrCeO_3$ (thickness, >1 Å) showing a Ruddlesden−Popper antiphase boundary (orthorhombic distortion omitted for clarity).

550−850 °C, in which no significant increase in the CeO_2 diffracting volume, and only vestiges of Sr_2CeO_4 at 850 °C, are observed. This temperature range corresponds to the operating regime of most electrochemical devices based on $SrCeO_3$, such as fuel-cell electrolytes and hydrogen-separation membranes; nevertheless, the acceptor-doped, proton-conducting $SrCe(M)O_{3-\delta}$ phases (M = trivalent dopant) may present rather different thermodynamic and kinetic characteristics from the parent phase.[41]

The SrO excess that is present in both nominally stoichiometric $SrCeO_3$ and XRD single-phase Sr superstoichiometric compositions ($x < 0.04$) appears to be located in the RP antiphase boundaries. These boundaries have a rock-salt-like arrangement of Sr and O, as shown schematically in Figure 7. This configuration is obtained by removing a CeO_2 plane ($\{0\ 1\ 0_p\}$) from the perovskite subcell and translating the adjacent SrO layer by half a unit cell along $\{0\ 1\ 0\}_p$, as observed in the HRTEM images of the $SrCeO_3$ series (Figure 5b). In addition to the similar irregular domain boundaries which have been found in the perovskite $BiMnO_3$,[27] Sr-rich RP defects have also been obtained in epitaxially grown $SrTiO_3/SrRuO_3$ bilayer films by introducing compositional fluctuations during film deposition.[28] The defects are reported to be associated with superdislocations which contribute to a misfit relaxation. The small amounts of SrO excess ($x \sim 0.03$) present in $SrCeO_3$ appear to give rise to embryonic intergrowth formation, which is stable for a limited compositional range. Longer range rock-salt perovskite intergrowth formation of the type which is exhibited in the well-known Ruddlesden−Popper series, e.g., $Sr_{n+1}Ti_nO_{3n+1}$, does not occur in the case of $Sr_{1+x}CeO_{3+\delta}$. Indeed, we find that the formation of Sr_2CeO_4 at high Sr concentrations occurs at a much lower limit ($x > 0.03$) than that reported by Chavan and Tyagi.[20]

The reversible formation of $Sr_{1.02}CeO_{3.02}$ at 1350 °C is an indication of the thermodynamic stability of the Sr-rich compositions at high temperature. The defective Sr-excess phases may, therefore, be of lower chemical potential than the ideal composition, such that $SrCeO_3$ does not form at high temperature, instead forming the Sr-rich phase. Indeed, it may be expected that the Sr-rich, RP defects introduce some misfit relaxation to the strained $SrCeO_3$ lattice. Alternatively, stoichiometric $SrCeO_3$ may be stable at high temperature but a partial, kinetically inhibited phase separation to the thermodynamically stable component oxides takes place on cooling, which accounts for the persistent presence of CeO_2 in the room-temperature phase analyses. However, we were unable to obtain phase-pure $SrCeO_3$ on quenching from 1250 to 1350 °C.

It is apparent that twinning and Sr-rich, RP planar defects are prevalent domain-boundary types in the parent phase of the $SrCeO_3$ proton-conducting family. It is worthwhile commenting that, frequently, the effects of such extended defects on ionic conductivity are considered unimportant or detrimental. However, higher diffusion rates and electrochemical activity have recently been observed in domain walls,[14,42,43] including twin boundaries and planar ordered defects. This has led to a more detailed understanding of domain boundaries in which localized phenomena, including the structure, elastic constants, charge, and vacancy concentration, have an important effect. As mentioned previously, the defect structure of the proton-conducting $SrCe(M)O_{3-\delta}$ series is likely to present additional microstructural complexities, such as oxygen-vacancy ordering and dopant-vacancy association.[4] The doped system therefore warrants a detailed microscopic study. Engineering of the microstructure may even enhance the electrochemical properties and realize the significant technological potential of this family of phases.

Conclusions

The apparent nonstoichiometry and structural defects of $SrCeO_3$ perovskite have been investigated, employing X-ray diffraction, selected area electron diffraction, high-resolution electron microscopy, and SQUID magnetic-susceptibility measurements.

Single-phase, Sr-superstoichiometric compositions $Sr_{1+x}CeO_{3+\delta}$ ($x = 0.02, 0.03$) may be readily synthesized by solid-state reaction, whereas the Dalton composition ($SrCeO_3$) is Sr rich. The Ce^{3+} content in the system is minor and does not influence the off-stoichiometry.

Electron diffraction confirms that the system crystallizes with the $GdFeO_3$-type orthorhombic perovskite structure (space group *Pnma*) in accordance with previous reports. Additional "concert" reflections are observed by electron diffraction, which are attributable to the combination of in-phase and anti-phase tilting of the CeO_6 octahedra.

(41) Matskevich, N. I.; Wolf, Th.; Stenin Yu., G.; Matskevich, M. Yu. *Themochim. Acta* **2006**, *444*, 107.

(42) Lee, W. T.; Salje, E. K. H.; Bismayer, U. *J. Phys.: Condens. Matter* **2003**, *15*, 1353.

(43) Kurumada, M.; Iguchi, E.; Savytskii, D. I. *J. Appl. Phys.* **2006**, *100*, 01.

The microstructure is characterized by domain boundaries consistent with Ruddlesden−Popper-type planar defects that accommodate excess SrO; twin domain boundaries are also prevalent. The SrO-rich defect structure may contribute to a relaxation of the strain associated with the thermodynamically unstable $SrCeO_3$ lattice. Phase separation does not progress significantly on annealing for extended periods in the temperature range 550−800 °C.

Acknowledgment. We thank the Ministerio de Educación y Ciencia (Spain) for funding the project MAT2004-03070-C05-05 and CAM for the project MATERYENER S-505/PPQ/0358. We also thank the Microscopy Centre "Luis Bru" at U.C.M. for technical assistance and Lina Carvalho for her assistance with ICP-AES analysis at the Central Laboratory in Aveiro.

IC701703C